PERGAMON

International Journal of Heat and Mass Transfer 44 (2001) 2727–2737

International Journal of HEAT and MASS TRANSFER

www.elsevier.com/locate/ijhmt

Paraffin/porous-graphite-matrix composite as a high and constant power thermal storage material

Xavier Py *, Régis Olives, Sylvain Mauran

C.N.R.S. – I.M.P., Institut de science et de génie des Matériaux et Procédés, 52 avenue de Villeneuse, 66860 Perpignan cedex, France

Received 6 February 2000; received in revised form 26 August 2000

Abstract

A new supported phase change material (PCM) made of paraffin impregnated by capillary forces in a compressed expansed natural graphite (CENG) matrix is presented. High loads of paraffin were obtained: from 65% to 95% weight depending upon the bulk graphite matrix density. Composite PCM/CENG thermal conductivities were found to be equivalent to those of the sole graphite matrix: from 4 to 70 W m^{-1} K^{-1} instead of the 0.24 W m^{-1} K^{-1} of the pure paraffin. Thermal power and capacity of the composite are theoretically compared to those of conventional systems in the case of two usual external geometries: tubes and spherical hollow nodules. The CENG induced a decrease in overall solidification time and a stabilization of the thermal storage power. An optimization procedure of the composite composition was proposed according to the antagonistic behaviours of the thermal power and the thermal capacity with respect to the CENG content. Within the usual external heat transfer coefficient range, the estimated CENG matrix optimized densities fell within the practicable range.

1. Introduction

Eight basic classes of thermal storage materials of organic and inorganic origins are known: liquids, rocks, soils, concretes, crystal hydrates, fatty acids, paraffins and eutectic compositions [1]. They are linked to three basic energy storage methods: sensible heat, latent thermal energy and chemical energy. In phase change energy storage, heat is stored by means of the latent heat of phase change of the medium. Gas–liquid phase change leads to extensive heat but also to a strong difference in respective phases volumes. Therefore, in such systems the gas phase has to be stored by absorption (H_2O/LiBr [2]), adsorption (H_2O/zeolite [3], CO_2/activated carbon [4]) or reaction (NH_3/salts [5]). Those systems are today at the stage of industrial prototypes [6] and present some specific interest like heat storage at ambient temperature and running free of vibration or noice. Nevertheless, they also present some disadvantages as complexity, use of advanced materials, toxicity or corrosion of the involved components and needs of very efficient heat exchangers. Liquid–solid phase change has been used for years: for example in 1892 sodium acetate was used in railway. They present today the sole widespread commercial application but still suffer from some limitations. The temperature of the liquid–solid phase change material (PCM) remains more or less constant during the phase transformation. Heat storage through PCM has the advantage of compactness because the heat of fusion (melting) of PCMs is very much larger than their specific (sensible) heats. The various PCMs are generally divided into two groups: organic and inorganic compounds. Inorganic compounds show a volumetric latent thermal energy storage capacity twice that of organic compounds [7]. Nevertheless, organic substances present several advantages including their ability to melt congruently, their self-nucleation and their non-corrosive behaviour. Alkanes, paraffins and waxes belong to the latter category. Their properties as PCM have been extensively studied by Himran et al. [7]. The melting points and the heats of fusion of alkanes increase with their number of carbon atoms (from C_1 to C_{100}) from 90.68 to 388.40 K and

* Corresponding author. Tel.: +33-04-68662110; fax: +33-04-68662141.

E-mail address: py@univ-perp.fr (X. Py).

0017-9310/01/$ - see front matter
PII: S0017-9310(00)00309-4

Nomenclature

d	diameter (m)
D	imbibition diffusivity ($m^2\ s^{-1}$)
e	nodule wall thickness (m)
g	gravitational acceleration ($m\ s^{-2}$)
h	heat transfer coefficient ($W\ m^{-2}\ K^{-1}$)
L	latent heat of fusion ($J\ kg^{-1}$)
P	thermal power per unit of length ($W\ m^{-1}$)
p	paraffin weight percentage (%)
Q	volumic thermal capacity per unit of length ($J\ m^{-4}$)
r	radius (m)
R	thermal resistance per unit of length ($m\ K\ W^{-1}$)
Ra	Rayleigh number (dimensionless)
S	saturation percentage (%)
t_s	solidification time (s)
T	temperature (K)
X	reduced solid front radius (r_f/r_{in}) (dimensionless)
z	paraffin–air interface depth within the CENG (mm)

Greek symbols

α	thermal diffusivity ($m^2\ s^{-1}$)
β	thermal expansion coefficient (K^{-1})
ΔP	pressure drop (Pa)
ε	bulk open porosity of the graphite matrix (dimensionless)
γ	contact angle (rad)
λ	thermal conductivity ($W\ m^{-1}\ K^{-1}$)
μ	dynamic viscosity (Pa s)
ρ	density ($kg\ m^{-3}$)
σ	surface tension ($N\ m^{-1}$)
θ	reduced solidification time (dimensionless)
v	cinematic viscosity ($m^2\ s^{-1}$)

Subscripts

a	axial
c	calculated
ex	external
f	phase change front
i	stone
in	internal
m	melt
o	cavity
p	paraffin
r	radial
s	solid phase
w	wall

from 58 to 285 kJ kg^{-1}, respectively. The family of *n*-alkanes has a large spectrum of latent heats, melting points, densities and specific heats so that they present a good flexibility for the heat storage designer. Paraffin waxes consist of mixtures of mainly normal alkanes. The amount of normal alkanes in a paraffin wax usually exceeds 75% and may reach almost 100% with the rest consisting of mostly iso-alkanes, cyclo-alkanes and alkyl benzene. Paraffin waxes are generally polydisperse compounds for which polydisperse solution theories must be used for characterization [8]. With knowledge about the thermophysical properties of pure alkanes and paraffin waxes, it is possible to design a thermal energy storage medium comprising these compounds.

Although paraffin waxes exhibit desirable properties as PCMs, they present a low thermal conductivity (0.24 $W\ m^{-1}\ K^{-1}$). This property reduces the rate of heat storage and extraction during melting and solidification cycles and therefore the overall power of the phase-change regenerator. In order to offset the low thermal conductivity of an alkane-based PCM, its container must be designed with an adequate surface-to-volume ratio and container material must have a suitable heat transfer coefficient. Consequently, several configurations have been studied: nodules [9–11], unfinned and finned cylinders [12,13], micro-encapsulation [14]. Those configurations lead to reduced effective energy storage capacity (50%) and container wall, usually made of polymers, induce additional and significative heat transfer resistance. The paraffin wax low thermal conductivity can also be enhanced by embedding a metal matrix stucture [7,13,15] or fins [1,13] in it. Nevertheless, such metal structures add significative weight and cost to the storage process. Other authors [16,17] have used water/paraffins emulsion of micronic size drops stabilized by emulsifier surfactant. The PCM hold up usually ranges from 10% to 50% vol and the needed amount of surfactant as much as 6–11% wt. The heat exchange is proceeded by direct bubbling of air through the suspension [17] leading to substantial gaz pressure drop or by flowing the non-Newtonian suspension through heat exchangers.

Some other authors have used paraffin waxes supported within the porous structure of silica catalyst [18] or activated carbon [19,20]. They have shown how the mean pore size of the support could be critical: if it is too small, the PCM molecular motion is hindered thereby adversely affecting latent heat storage capacity; if the pores are too large, there is insufficient capillary force to retain the liquid wax. In the particular case of activated carbons, waxes are well retained in micropores but lose their phase change properties while waxes retained in macropores present significative exudation tendency. Consequently, optimum texture of activated carbon for

this application would be mesoporous. However, those two porous supports do not present real improvement of the effective thermal conductivity: the order of magnitude of the thermal conductivity of silica supports and activated carbon is 0.2 W m^{-1} K^{-1} [21,22].

Such a limitation due to the low thermal conductivity of the involved material has been already solved for solid–gas chemical storage systems developed by the laboratory for years [23]. In those systems, low conductive reactive salts are supported by a porous graphite matrix the thermal conductivity of which ranges from 4 to 100 W m^{-1} K^{-1}. This support presents also additional advantages as high external heat transfer coefficient values (from 500 to 3000 W m^{-2} K^{-1}), very low bulk density (from 50 to 350 kg m^{-3}) good mechanical properties and chemical inertness. It is known to be superior to porous metallic foams made of aluminium, copper or nickel [24]. Various shapes are easily molded from expanded graphite powders allowing perfect contact between the composite and any reactor or exchanger wall.

The aim of the present study is to apply this knowledge to supported PCMs materials and especially to paraffin waxes in order to abolish some of their disadvantages and to propose controlled high power supported PCMs.

2. Experimental investigation

2.1. Investigated materials

Expanded graphite powder was supplied by Le Carbone Lorraine at a bulk density of 3 kg m^{-3}. Two commercial paraffins of different melting temperatures (Aldrich paraffin wax 41167-1: $T_m = 73$–$80°C$, $\rho = 915$ kg m^{-3}; Fluka paraffin wax 76234: $T_m = -9°C$, $\rho = 870$ kg m^{-3}) and the hexadecane (99% Aldrich H670-3: $T_m = 18.1°C$, $\rho = 773$ kg m^{-3}) were tested. Two paraffins of intermediate melting temperatures supplied by Prolabo ($T_m = 51$–$53°C$ and $T_m = 60$–$62°C$) were also experimented and led to similar results. Therefore, only results obtained for the three first PCMs are presented in the paper.

2.2. PCMs/CENG composite material elaboration

Expanded graphite powders were poured into a cubic mold of aluminium and then pressed to obtain the porous graphite matrix with the desired bulk density. The interlocking of expanded graphite powders produces a cohesive compact without a binder. Graphite matrices cubic in shape (25×10^{-3} m) were prepared with bulk densities ranging from 50 to 350 kg m^{-3}. The lower density value was linked to the usual acknowledged limit of mechanical strength of the matrix and the higher density to values of permeability and available porosity at which impregnation kinetics and PCM capacity started to become too low.

Each cubic matrix was soaked into melted paraffin and regularly weighted until maximum load was reached. At low bulk density of the graphite matrix or for short chain paraffins, a strong gaseous release was observed in the form of small bubble ropes from the external surface. For higher bulk graphite matrix densities, a small gaseous release was observed in the form of continuous small bubble ropes discharged from only few radial sites. It seemed that in that case, the impregnation was the result of a lack of homogeneity in external surface permeability: few spots of relatively high permeability were responsible for the impregnation.

In Fig. 1 were illustrated the soaking curves of the hexadecane in CENG matrix of five densities from 48 to 182 kg m^{-3} in terms of saturation percentage S which is calculated on the basis of the ratio between the hexadecane volume and the available porous volume of the matrix. The hexadecane loading speed is very fast during the first hundred seconds and then decreases down gradually to reach an asymptotic linear behaviour. After 3000 s, the saturation ranges between 35% and 80% depending on the CENG matrix density.

The hexadecane penetration within the matrix porosity is due to capillarity. The pressure drop through the moving interface can be conventionally expressed by means of the Laplace law:

$$\Delta P = 2\sigma\cos(\gamma)/r, \tag{1}$$

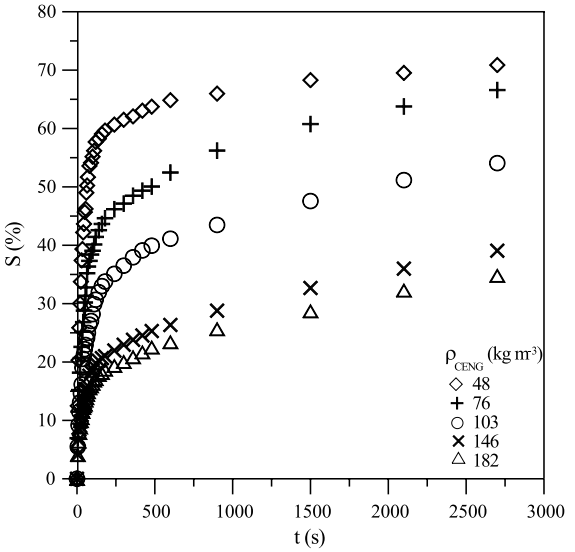

Fig. 1. Saturation curves for hexadecane and five different CENG densities.

where σ is the interfacial tension, γ the contact angle and r is the mean pore radius. This pressure drop is balanced by the pressure drop due to the gravity. From the Hagen–Poiseuille equation, one can express the hexadecane–air interface displacement leading to the Washburn law:

$$dz/dt = r^2/(8\mu z)(2\sigma\cos(\gamma)/r - \rho g z). \quad (2)$$

At the beginning of the loading, the gravity effect is negligible compared to the capillary one. The last equation can be integrated leading to,

$$z = (Dt)^{1/2} \quad (3)$$

with,

$$D = \sigma r\cos(\gamma)/2\mu \quad (4)$$

which is an effective diffusivity related to the soaking phenomenon.

Assuming the CENG matrix perfectly wet by the hexadecane, the contact angle γ is equal to zero. From the obtained Eqs. (3) and (4), the mean pore radius of the different CENG matrix was identified using the first soaking period. This was illustrated in Fig. 2 by the good linearity of z^2 versus time at low soaking time.

The mean pore radius values identified from the slopes of the obtained linear curves led to the following empirical law,

$$r = r_o(\rho_{CENG}/\rho_{CENGo})^{-1.4}, \quad (5)$$

where $r_o = 3.8 \times 10^{-6}$ m and $\rho_{CENGo} = 46$ kg m^{-3} are the mean pore size and the density of the isotropic matrix, respectively.

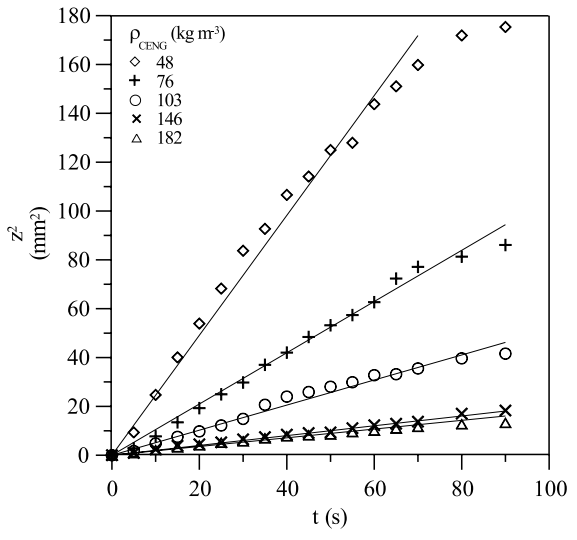

Fig. 2. Paraffin penetration depth versus time for various bulk CENG densities.

This last expression has to be compared to the corresponding measurements obtained by conventional mercury porosimetry method [25] leading to,

$$r = r_o(\rho_{CENG}/\rho_{CENGo})^{-2.1} \quad \text{with} \quad r_o = 0.5 \times 10^{-6} \text{ m}. \quad (6)$$

Therefore, the pore radius measured by mercury imbibition presents larger values than those obtained by hexadecane imbibition. This difference is probably due to the fact that the hexadecane–CENG contact angle could present a value different than zero. Nevertheless, Eqs. (3)–(5) can be used for paraffin/CENG imbibition kinetics estimation.

Concerning the present study, the impregnation characteristic time was low enough and paraffins were incorporated by simple capillary forces instead of more costly vacuum impregnation. Nevertheless, especially for long-chain paraffins presenting high values of viscosity or for high bulk density graphite matrix, impregnation kinetics could become too low and could require more sofisticated process like vacuum protocole especially for industrial elaboration.

2.3. PCMs/CENG composite composition

Maximum observed paraffin loads were compared to calculated theoretical amount of paraffin which could be incorporated if all the porosity was filled. For a specific bulk density of the graphite matrix, the total porosity was calculated by the following equation:

$$\varepsilon = \rho_{CENG}(1/\rho_{CENG} - 1/2250), \quad (7)$$

where 2250 kg m^{-3} was the theoretical density of graphite [25].

Nevertheless, a small amount of this porosity, from 3% to 10% vol, was known [26] to be closed porosity and consequently could not be filled by paraffin. In Fig. 3 were compared the experimental weight percentages of impregnated paraffins to calculated values assuming no closed porosity and assuming 10% vol of closed porosity.

The obtained results (see Fig. 3) showed clearly that the measured paraffin weight fractions fell within the theoretical open and available loaded porosities. Therefore, the obtained imbibition data were in agreement with the usual amount of closed porosity acknowledged to range from 3% to 10% vol.

In terms of capacity and depending on bulk graphite density, the CENG/paraffin composites present a weight percentage ranging from 65% to 95% and a corresponding volume percentage of 60–90%. Consequently, the CENG support allowed very high PCMs loadings.

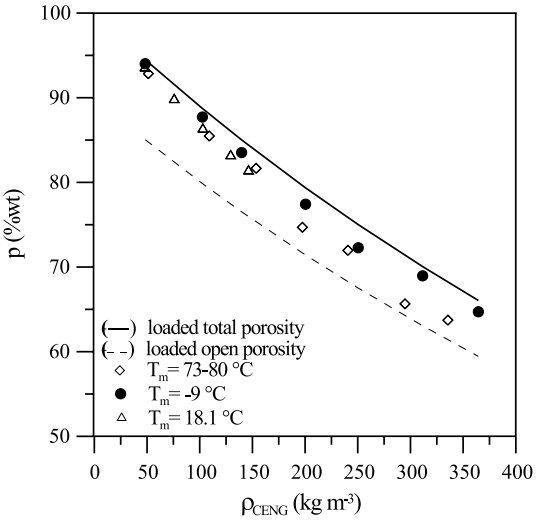

Fig. 3. Maximum hexadecane weight loading versus bulk graphite matrix density for three paraffins.

2.4. Thermal conductivity measurement

A steady-state measurement apparatus, illustrated elsewhere [27], was used for thermal conductivity measurement of the composites in their cubic shape ($25 \times 25 \times 25$ mm^3). The experimental device was composed of two plates, one heat source and one heat sink, made of aluminium alloy which temperatures were regulated and two flux-meters made of rods ($25 \times 25 \times 65$ mm^3) of well-known conductivities. The axial temperature profile measured by K-type thermocouples implanted in the two flux-meters and in the sample placed between them, was recorded. A polystyrene foam ($\lambda = 3 \times 10^{-2}$ W m^{-1} K^{-1}) has been chosen as an insulator in order to reduce the radial heat losses and to obtain a quasi one-dimensional heat flow. In this way, Fourier's first law was used to estimate the thermal conductivity [28]. The measurement accuracy was about 10% and was mainly limited by the uncertainty of the thermocouples positions in the sample. This apparatus allowed measurements of conductivity in the range from 0.3 to 200 W m^{-1} K^{-1}. Moreover, the thermal contact between the sample and the two flux-meters was controlled by an external axial pneumatic compression. Therefore, no conductive paste was added at the thermal interfaces.

2.5. PCMs/CENG composites thermal conductivities

The thermal conductivity of the porous graphite matrix is known to be improved when its bulk density is increased. One of the most particular properties of the porous graphite matrix is its anisotropy in the thermal conductivity depending upon the direction. Thermal conductivity in the axial direction (parallel to the compression force) is in the range of 4–10 W m^{-1} K^{-1} depending upon the bulk density and that in radial direction (perpendicular to the compression force) is in the range of 5–100 W m^{-1} K^{-1}. This anisotropy has been reported by several authors with different values [24,29]. As thermal conductivity depends only on the carbon content or void volume, this lack of agreement between published results could be due to differences in graphite origin, compression conditions or thermal conductivity measurements methods. However, this anisotropy is attributable to the alignment of the basal planes in graphite crystals. Note that the thermal conductivity of this graphite single crystal varies from 10 (c-axis) to 2000 (a-axis) W m^{-1} K^{-1}. Due to the irregularity of the microstructure, a confident prediction of the thermal conductivity becomes quite difficult and only empirical correlations are availables [29,30].

Experimental conductivities of paraffin/CENG composites and calculated conductivities of raw CENG with respect to the axial and radial directions in Fig. 4 were illustrated. Obviously, the overall thermal conductivity of the composites was similar to that of the sole porous graphite matrix. Therefore the very low thermal conductivity of paraffin (0.24 W m^{-1} K^{-1}) did not affect the overall one despite very high paraffin impregnation level (as high as 96% wt). Consequently, the thermal conductivity of the paraffin/CENG composite can be easily and directly estimated from CENG available correlations:

$$\lambda_a = 3.0(\rho_{CENG}/46)^{2/3}\left[2 - (\rho_{CENG}/46)^{0.17}\right], \quad (8)$$

$$\lambda_r = 3.0(\rho_{CENG}/46)^{4/3+0.17}. \quad (9)$$

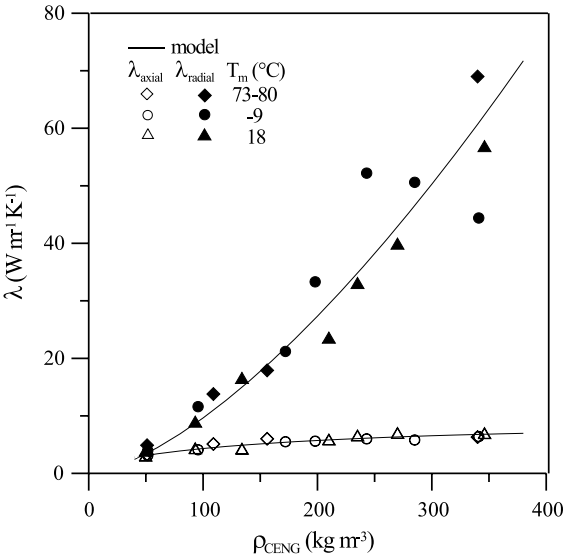

Fig. 4. Paraffin/CENG and raw CENG axial and radial thermal conductivities versus bulk graphite matrix density.

Therefore, the thermal characteristics of those composites can be easily managed upon the desired process power.

Moreover, some authors [13,19,20] have published results on the optimization in storage process using thermal stratification. This phenomenon, resulting in inhomogeneity in temperature within the storage media, could be improved by the thermal conductivity anisotropy of the elaborated composite.

3. Theoretical investigation

In order to compare the thermal storage capacity and the effective thermal power of the paraffin/CENG composites to the corresponding raw PCM, calculations were done at the process level taking into account the different components and thermal resistances. As illustrated in Fig. 3, CENG composites present high intrinsic thermal storage capacity. Moreover, the fins usually used for extension of the specific area needed for heat transfer are not required anymore thanks to the high thermal conductivity of the PCM/CENG composite. Consequently, at the process level, the PCM effective capacity and performances should be improved in case of using the composite in spite of the volume filled by the pure CENG.

Two different geometries of storage volumes have been extensively studied in the literature: the horizontal or vertical multi-tube system [12] and the spherical hollow nodules [10]. In the former case, the energy balance presents an analytical solution while in the last case only a numerical solution is admitted. Moreover, a uniform radial conductivity of a CENG matrix is easily made in cylindrical shape while it is technically very difficult to obtain in spherical shape. Therefore, the following calculations are concerned with the tube geometry but same numerical results were obtained in the case of spherical hypothetical nodules. Cylindrical hollow nodule made of copper, as described in [12], was considered with an external diameter and a wall thickness of 3.2×10^{-2} m and 10^{-3} m, respectively. With respect to the cylindrical geometry, all calculations were done on the basis of a unit of length of the tube. The process parameters, external to the nodule, were the surrounding heat-transfer fluid (HTF) temperature T_{ex} set at 10 K from the melting temperature of the PCM and the external heat transfer coefficient h_{ex} ranging from 100 to 350 W m^{-2} K^{-1}.

3.1. Cool-storage step model

PCM based cool-thermal storage units present local working power P per unit of length of tube as a function of three successive thermal resistances:

$$P = (T_m - T_{ex})/(R_{ex} + R_w + R_{in}) \tag{10}$$

in which the resistance of the external fluid per unit of length of tube is expressed by,

$$R_{ex} = (2\pi r_{ex} h_{ex})^{-1} \tag{11}$$

the resistance respective to the copper wall,

$$R_w = (2\pi\lambda_w)^{-1} \ln(r_{ex}/r_{in}) \tag{12}$$

and the solid PCM resistance which thickness is time dependent:

$$R_s = -(2\pi\lambda_{in})^{-1} \ln(X), \tag{13}$$

where X is the reduced radius of the solidification front moving from the internal surface of the nodule wall ($X = 1$) to the centre of the nodule ($X = 0$).

Those resistances being in series, the overall thermal resistance is expressed by,

$$R = R_{ex} + R_w + R_s. \tag{14}$$

Being linked to the moving reduced radius X, the effective power of the nodule is time dependent and mainly limited by internal limitations induced by the already solidified PCM.

The basic equation used for calculation of the front position with respect to time was the heat energy balance assuming that all heat produced by the solidification at X is withdrawn toward the external fluid [9,10]:

$$2\pi r_f \varepsilon \rho_s L \, dr_f = -P \, dt \tag{15}$$

this last equation linked to the expression of the overall heat power P (Eq. (10)), led to the solidification duration needed to reach the reduced radius X:

$$t(X) = -\int_1^X 2\pi\varepsilon\rho_s L r_{in}^2 y (T_m - T_{ex})^{-1} \times [R_w - (2\pi\lambda_{in})^{-1} \ln(y) + R_s] \, dy. \tag{16}$$

This expression admits an analytic solution:

$$t(X) = X^2/2[A + B(\ln(X) - 1/2)] - (A - B/2)/2, \tag{17}$$

where

$$A = -\varepsilon\rho_s L r_{in}^2 (T_m - T_{ex})^{-1} [(r_{ex}\lambda_{ex})^{-1} + \ln(r_{ex}/r_{in})/\lambda_w],$$
$$B = \varepsilon\rho_s L r_{in}^2/[\lambda_{in}(T_m - T_{ex})]. \tag{18}$$

The duration time needed for complete solidification of the PCM in the nodule is calculated for $X = 0$ and labelled t_s.

$$t_s = \varepsilon\rho_s L r_{in}^2 [1/(2\lambda_{in}) + 1/(r_{ex}h_{ex}) + \ln(r_{ex}/r_{in})/\lambda_w][2(T_m - T_{ex})]^{-1}. \tag{19}$$

The reduced solidification time θ is equal to the ratio of $t(X)$ and t_s. The maximum duration time t_{max} was calculated in the case of pure PCM without CENG and $X = 0$. The maximum heat storage Q_{max} was calculated for pure PCM and 100% loaded nodule.

3.2. Thermal resistances

As the PCM solidification front is moving from the inner surface of the wall to the centre of the nodule, the released heat has to move towards the opposite direction through the already solidified PCM. Therefore, during the solidification step, the thermal resistance of the solid PCM increases while the solidification front area decreases. This effect is illustrated in Fig. 5 by plotting the solid PCM resistance R_s to the overall thermal resistance R against the reduced solidification time θ for various CENG densities and pure PCM. For such calculations, the external HTF coefficient was set at 200 W m^{-2} K^{-1} according to the average conditions used in the referenced paper. Without CENG, the solid PCM contribution to the overall thermal resistance increases sharply from 5% to 83% the first 20% of the reduced solidification time. The CENG brings down the initial thermal resistance to the sole contribution of the nodule wall and reduces the slope and the behaviour of the curve significantly. For an intermediate value of CENG bulk density of 163 kg m^{-3}, a tremendously reduced PCM contribution of only 12% to the total thermal resistance is reached at 80% of the reduced solidification time. At higher CENG densities, the whole solidification step proceeds with a solid contribution to the heat transfer resistance lower than 20%.

3.3. Nodule overall power

As already mentioned, during the cool-storage step, the PCM solidification front is moving from the inner surface to the centre of the nodule and the heat has to move in the opposite direction through the already solidified PCM. Therefore, during the solidification step, the thermal resistance of the solid PCM increases and, according to Eq. (10), the overall power of the nodule decreases. As illustrated in Fig. 6, this effect is particularly pronounced in the case of nodule filled with pure paraffine. In this case, the initial value of the overall power per unit of length is decreased to half after only 5% of the total solidification time. In comparison, nodules filled with composite at the minimum of CENG content present a similar power reduction at 80% of the solidification time. At CENG densities higher than 350 kg m^{-3}, the solid PCM effect on the overall power is fairly negligible and the nodule presents a stabilized thermal power. Such stable behaviour should be of great interest by simplification of the design procedures. In terms of mean overall power per unit of lenght, the use of such a CENG density induces an enhancement up to 3 compared to pure paraffin. In the Fig. 7, the same data were illustrated versus dimensional solidification time for comparison. This illustrates the important reduction in overall solidification time induced by the CENG. By an increase in CENG density from 50 to 200 kg m^{-3}, the overall solidification time is reduced of a third. Moreover, when using CENG, the final solidification time is easily defined while it presents only an asymptotic value in case of pure PCM. This leads to best overall performances and easiness in process design and optimization.

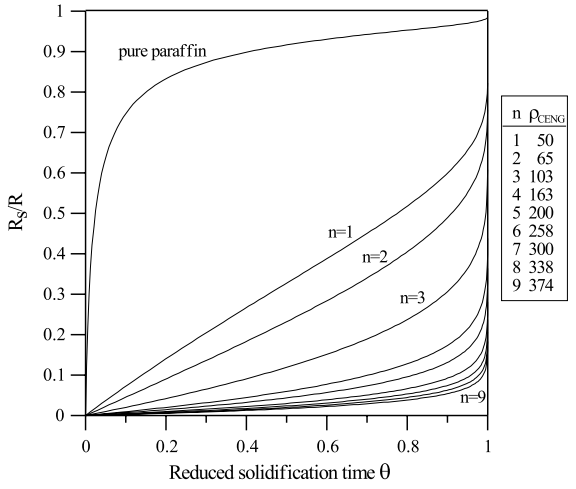

Fig. 5. Solid PCM thermal resistance contribution to total thermal resistance versus reduced solidification time for pure paraffin ($n = 0$) and various CENG contents ($n > 0$).

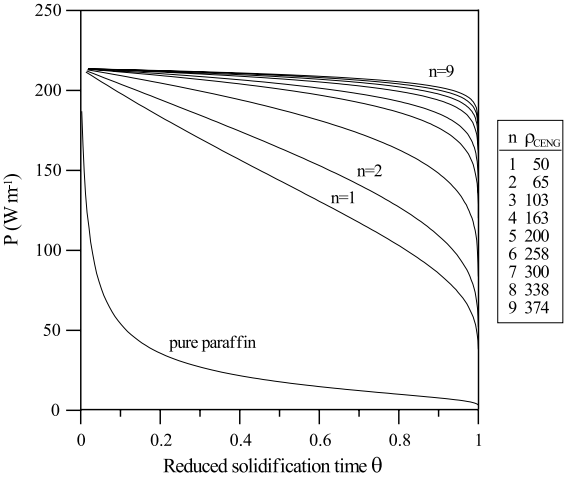

Fig. 6. Nodule overall power versus reduced solidification time for pure paraffin ($n = 0$) and various CENG bulk densities ($n > 0$).

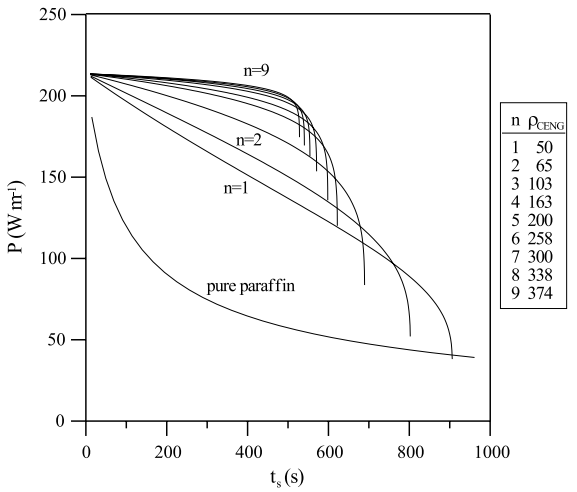

Fig. 7. Nodule overall power versus dimensional solidification time for pure paraffin ($n = 0$) and various CENG bulk densities ($n > 0$).

3.4. CENG density optimization

As previously mentioned, thermal conductivity and open porosity of porous graphite matrix present opposite behaviours with respect to CENG bulk density. Consequently, overall nodule power and storage capacity present also opposite trends with respect to the CENG amount. This is illustrated in Fig. 8 in which reduced power and reduced capacity per unit of length were calculated as being the ratios of effective values to those obtained without CENG and plotted versus CENG bulk density in the case of $h_{ex} = 200$ W m^{-2} K^{-1}. At increasing CENG content from 50 up to 200 kg m^{-3}, the reduced power increases sharply (from 60% to 90%) while the PCM capacity decreases linearly but slightly (10% in decrease). At higher CENG contents, the increase in reduced power is slight while the decrease in PCM capacity follows its above-mentioned linear behaviour. Thus, for any particular application, those effects lead to an optimum value of the CENG bulk density with respect to the respective importances given to both criteria, the reduced thermal power and thermal capacity. In the present study, this optimization has been studied given the same importance to the two concerned goals. In Fig. 9, the absolute value of the difference between the reduced power and the reduced capacity, taken as optimization criteria and written Op (Eq. (20)), was plotted versus CENG density for various external h_{ex} values from 100 to 350 W m^{-2} K^{-1} (Fig. 9).

$$\mathrm{Op} = |P/P_{\mathrm{PCM}} - Q/Q_{\max}|. \tag{20}$$

The minimum of each curve corresponds to the optimum CENG density. An increase in external heat transfer coefficient h_{ex} induced an increase in overall thermal power and then, an increase in optimized CENG bulk density. In Fig. 10, those optima were plotted against the external heat transfer coefficient h_{ex} within the considered range. The obtained optima CENG densities (from 70 to 145 kg m^{-3}) fall within the usual practicle values (between 50 and 350 kg m^{-3}).

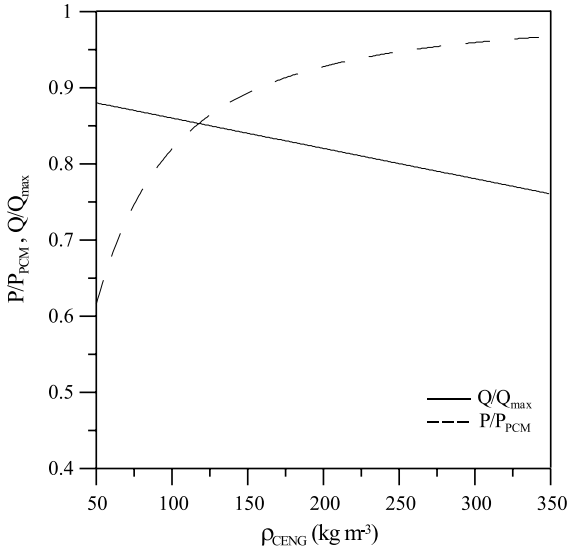

Fig. 8. Reduced overall power and reduced thermal capacity of the nodule versus the CENG matrix density, $h_{ex} = 200$ W m^{-2} K^{-1}.

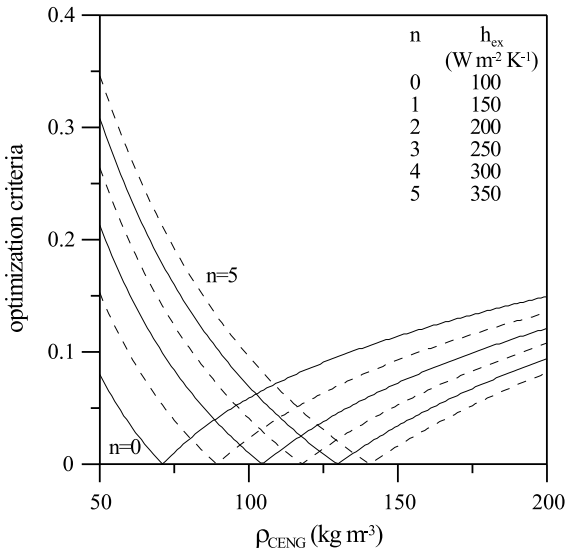

Fig. 9. Optimization criteria (Eq. (20)) versus CENG bulk density for various external heat transfer coefficient values.

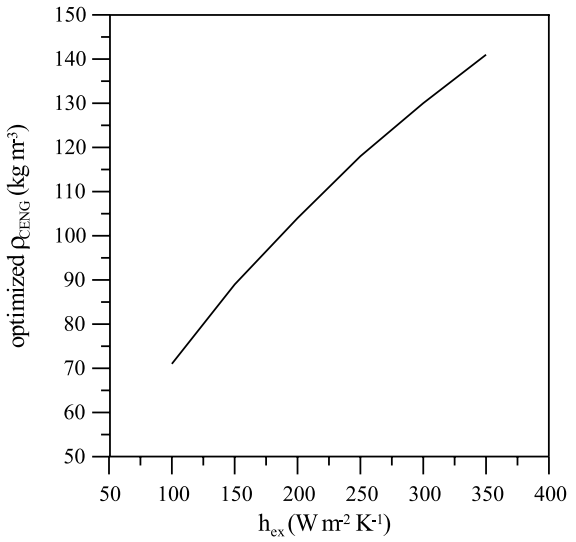

Fig. 10. Optimized CENG bulk densities versus external heat transfer coefficient.

Moreover, the optimum PCM/CENG composition depends on the wall thickness and/or on its thermal conductivity. Therefore, the nodule overall performances should be optimized through the simultaneous optimizations of all the components.

3.5. Overall process optimization

Considering the HTF, one has to take into account its pressure drop as one of the main process parameters. In that case, gain could be taken considering the fact that various shapes are easily molded from expanded graphite powders and optimum shape with respect to pressure drop could be optimized as shown by Fowler et al. [31].

3.6. Melting step

In order to take advantage of the already published studies, all the above calculations were concerned by the sole solidification mode. Nevertheless, the melting mode has to be considered too. In this case, the free convection in the region between the wall and the melting front could induce enhancements of heat flux and front velocity. In the case of PCM/CENG, such phenomenon could be inhibited by the dispersion of the paraffin in the porous matrix. The estimation of the modified Rayleigh number Ra^* [32] leads to the extent of effective free convection in the CENG cavity. In order to simplify the system, the CENG cavity is assimilated to a hollow sphere in which the PCM is melting concentrically as a spherical stone.

The modified Rayleigh number is expressed by

$$Ra^* = (D_o - D_i)Ra(D_oD_i)^{-4}(D_o^{-7/5} + D_i^{-7/5})^{-5}, \quad (21)$$

where

$$Ra = g\beta(T - T_m)(D_o - D_i)^3/\alpha v. \quad (22)$$

The difference in temperature between the CENG wall and the melting front was taken equal to 2.5 K. The order of magnitude of the characteristic diameter of the CENG cavity (D_o) is 50×10^{-6} m [26], the diameter of the solid paraffin stone (D_i) is taken equal to half of D_o. The various properties of the paraffin at 293.75 K were estimated using the methods gathered by Reid et al. [33]: $\alpha = 8.5 \times 10^{-8}$ m^2 s^{-1}, $v = 4 \times 10^{-6}$ m^2 s^{-1}, $C_p = 2.215$ J kg^{-1} K^{-1}. The order of magnitude of the thermal expansion coefficient was based on the available value for *n*-octadecane [34]: $\beta = 0.9 \times 10^{-3}$ K^{-1}.

Those values led to the following estimation of the modified Rayleigh number,

$$Ra^* \approx 1.3 \times 10^{-5}. \quad (23)$$

According to referenced critical values [32], estimated Ra^* is very small before 100 and the effective heat transfer between the CENG wall and the PCM stone through the melted PCM is free of natural convection. Thus, the porous matrix should inhibit the possible heat transfer enhancement induced by free convection but simultaneously offers high surface area and high thermal conductivity. The second and third effects are obviously much stronger than the former. Moreover, this inhibition linked to the fact that thermal conductivity of the composite is equal to the conductivity of the CENG, leads to the advantage of having similar heat power under solidification and fusion mode. Therefore, no additional calculations are needed for CENG/PCM in the melting mode.

4. Conclusions

New paraffin/CENG composites of high thermal conductivity have been elaborated and characterized. The paraffin is maintained by capillary forces within the whole open available porosity of the porous graphite matrix leading to high paraffin weight percentage up to 95% wt. The imbibition data of the PCM within the CENG matrix were well correlated by the conventional Washburn law leading to mean pore size values lower than those measured by the deforming mercury porosimetry method. The thermal conductivity of the composite has been found to be equal to that of the sole porous graphite matrix (4–70 W m^{-1} K^{-1}) and to present the same anisotropy with respect to the compression axis. Therefore, the very low thermal conductivity of the paraffin (0.24 W m^{-1} K^{-1}) did not affect the

performances of the composite. As porosity and thermal conductivity are opposite functions of the graphite bulk density, optimum value of this parameter will be associated to each particular thermal storage application. Compared to conventional PCMs, in case of processes composed of cylindrical or spherical hollow nodules, PCM/CENG composites led to high and stable thermal power and easily defined phase change duration. Therefore, thermal storage processes using such composite materials could be designed and managed much more easily. Moreover, according to an estimated value of the modified Rayleigh number smaller than 100, free convection through the melted PCM is inhibited by the CENG cavities. Nevertheless, CENG high thermal conductivities offset and then exceed significantly this effect. Further studies will be done in experimental thermal storage application using various shapes of packing.

Acknowledgements

The authors acknowledge the financial support of the European Community through the contract Joule III JOE3-CT98-0055.

References

[1] K.S. Shakhabov, A.V. Tkachev, O.A.M. Khashiev, Use of paraffin compositions as thermal-storage substances in solar heat treatment of reinforced-concrete items, Geliotekhnica 26 (1990) 69–72.

[2] Z. Lu, L. Fan, W. Cao, D. Li, Development of absorption technologies with lithium bromide in China, in: Proceeding of the ISHPC, Munich, Germany, 1999, pp. 45–49.

[3] R. Lang, M. Roth, M. Stricker, Development of a modular zeolite–water heat pump, in: Proceeding of the ISHPC, Munich, Germany, 1999, pp. 611–618.

[4] S. Follin, V. Goetz, A. Guillot, Influence of microporous characteristics of activated carbons on the performance of an adsorption cycle for refrigeration, Ind. Eng. Res. 35 (1996) 2632–2639.

[5] V. Goetz, B. Spinner, Cooling with a sorption process in a high temperature environment, in: Proceeding of the ISHPC, Munich, Germany, 1999, pp. 591–595.

[6] X. Py, B. Spinner, F. Kindbeiter, L. Rigaud, Production de froid par systèmes thermo-chimiques solide–gaz, Revue Générale du Froid 989 (1998) 55–60.

[7] S. Himran, A. Suwono, Characterization of alkanes and paraffin waxes for application as phase change energy storage medium, Energy Sources 16 (1994) 117–128.

[8] G.A. Mansoori, P.C. Du, E. Antoniades, Equilibrium in multiphase polydisperse fluids, Int. J. Thermophy. 6 (1989) 1181–1204.

[9] J.P. Bedecarrats, F. Strub, B. Falcon, J.P. Dumas, Phase-change thermal energy storage using spherical capsules: performance of a test plant, Int. J. Refrig. 19 (1996) 187–196.

[10] J.P. Bedecarrats, J.P. Dumas, Etude de la cristallisation de nodules contenant un matériau à changement de phase en vue du stokage par chaleur latente, Int. J. Heat Mass Transfer 40 (1997) 149–157.

[11] J.M. Buchlin, P.H. Theunissen, Stokage de chaleur dans une matrice compacte de matériau a changement de phase encapsulé, colloque Le génie chimique et le stokage de l'énergie, La société de Chimie Industrielle, 238e Manifestation de la Fédération Européenne du Génie Chimique 21 (1980) 1–10.

[12] H.W. Ryu, S.A. Hong, B.C. Shin, S.D. Kim, Heat transfer characteristics of cool-thermal storage systems, Energy 16 (1991) 727–737.

[13] S.M. Hasnain, Review on sustainable thermal energy storage technologies, Part I: heat storage materials and techniques, Energy Convers. Mgmt. 11 (1998) 1127–1138.

[14] M. Goel, S.K. Roy, S. Sengupta, Laminar forced convection heat transfer in microcapsulated phase change material suspensions, Int. J. Heat. Mass Transfer 37 (1994) 593–604.

[15] J. Huetz, Stokage de courte durée chaleur latente et de réaction, Colloque International, Stokage de l'Energie Solaire Appliquée au Bâtiment, Lyon K1-K12, 1981.

[16] J. Larue, Stockage thermique par émulsion, in: Proceedings of Le Génie Chimique et le stockage de l'énergie, 1980, pp. 22/1–22/4.

[17] H. Inaba, S.I. Morita, Cold heat-release characteristics of phase-change emulsion by air–emulsion direct-contact heat exchange method, Int. J. Heat Mass Transfer 39 (1996) 1797–1803.

[18] H.F. Erk, M.P. Dudukovic, Phase-change heat regenerators: modeling and experimental studies, AIChE J. 42 (1996) 791–808.

[19] C. Chapotard, D. Tondeur, Stockage de chaleur en lit fixe de charbon actif imprégné de paraffine. Expériences à petites échelles et approche simplissime, Entropie 107–108 (1982) 112–121.

[20] C. Chapotard, D. Tondeur, Dynamics of latent heat storage in fixed beds, a non-linear equilibrium model, the analogy with chromatography, Chem. Eng. Commun. 24 (1983) 183–204.

[21] H. Bjurstrom, E. Karawacki, B. Carlsson, Thermal conductivity of a microporous particulate medium: moist silica gel, Int. J. Heat Mass. Transfer 27 (1984) 2025–2036.

[22] G. Cacciola, G. Restuccia, L. Mercadante, Composites of activated carbon for refrigeration adsorption machines, Carbon 33 (1995) 1205–1210.

[23] S. Mauran, P. Prades, F. L'haridon, Heat and mass transfer in consolidated reacting beds for thermochemical systems, Heat Recovery Systems & CHP 4 (1993) 315–319.

[24] M. Groll, Reaction beds for dry sorption machines, Heat Recovery Systems & CHP 13 (1993) 341–346.

[25] R. Olivès R, Transfert thermique dans une matrice de graphite poreuse, consolidée et anisotrope, support d'un solide actif pour procédés énergétiques, Ph.D. Thesis, University of Perpignan, Perpignan, France, 1999.

[26] L. Rigaud, Ecoulement de gaz en régime permanent et transitoire à travers des milieux poreux composites graphite-sel pour transformateurs thermochimiques. Correlations entre perméabilité et structure, Ph.D. Thesis, IMP-CNRS, University of Perpignan, Perpignan, France, 1997.

[27] Y.S. Touloukian, R.W. Powell, C.Y. Ho, P.G. Klemens, Thermal conductivity. In Thermophysical Properties of Matter, vol. 2, IFI/Plenum, New York, 1970, pp. 1a–39a.
[28] H.S. Carslaw, J.C. Jaeger, In Conduction of Heat in Solids, 2nd ed., Oxford University Press, Oxford, 1959, p. 139.
[29] J.H. Han, K.W. Ho, K.H. Lee, H. Kim, Porous graphite matrix for chemical heat pumps, Carbon 36 (1998) 1801–1810.
[30] R. Olives, S. Mauran, Transfert thermique dans un matériau composite graphite/sel de grande porosité, in: Proceedings of the SFT 98 Thermique et environnement, Elsevier, Amsterdam, 1998, pp. 175–180.
[31] A.J. Fowler, A. Bejan, Correlation of optimal sizes of bodies with external forced convection heat transfer, Int. Commun. Heat Mass Transfer 21 (1994) 17–27.
[32] F.P. Incropera, D.P. DeWitt, in: C. Robichaud (Ed.), Fundamentals of Heat and Mass Transfer, Wiley, New York, 1996 (Chapter 9).
[33] R.C. Reid, J.M. Prausnitz, B.E. Poling, in: B. Sun, G.H. Fleck (Eds.), The Properties of Gases & Liquids, McGraw-Hill, New York, 1987.
[34] C. Benard, D. Gobin, F. Martinez, Melting in rectangular enclosures: experiments and numerical simulations, J. Heat Transfer 107 (1985) 794–803.